Drivers controlling black carbon temporal variability in the lower troposphere of the European Arctic

Stefania Gilardoni[1], Dominic Heslin-Rees[2], Mauro Mazzola[3], Vito Vitale[3], Michael Sprenger[4], and Radovan Krejci[2]

[1]Institute of Polar Science, National Research Council, Milan, 20156, Italy
[2]Department of of Environmental Science, Stockholm University, Stockholm, S 106 91, Sweden
[3]Institute of Polar Science, National Research Council, Bologna, 4018, Italy
[4]Institute for Atmospheric and Climate Science, ETH Zurich, Zurich, 8092, Switzerland

Correspondence: Stefania Gilardoni (stefania.gilardoni@cnr.it)

Abstract. Black carbon (BC) is a short-lived climate forcer affecting Arctic climate through multiple mechanisms, which vary substantially from winter to summer. Several models still fail in reproducing BC seasonal variability, limiting the ability to fully describe BC climate implications. This study aims at gaining insights into the mechanisms controlling BC transport from lower latitudes to the Arctic lower troposphere. Here we investigate the drivers controlling black carbon daily and seasonal variability in the Arctic using Generalized Additive Models (GAM). We analysed equivalent black carbon (eBC) concentration measured at the Gruvebadet Atmospheric Laboratory (GAL - Svalbard archipelago) from March 2018 to December 2021. The eBC showed a marked seasonality with higher values in winter and early spring. The eBC concentration averaged 22 ± 20 ng m^{-3} in the cold season (November - April) and 11 ± 11 ng m^{-3} in the warm season (May - October). The seasonal and interannual variability was mainly modulated by the efficiency of wet scavenging removal during transport towards the higher latitudes. Conversely, the short-term variability was controlled by boundary layer dynamics, local-scale, and synoptic-scale circulation patterns. During both the cold and the warm season, the transport of air masses from Europe and northern Russia was an effective pathway for the transport of pollution to the European Arctic. Finally, in the warm season we observed a link between the intrusion of warm air from lower latitudes and the increase in eBC concentration. Changes in synoptic scale circulation system and precipitation rate in the northern hemisphere, linked to climate change, are expected to modify BC burden in the Arctic.

1 Introduction

Black carbon (BC) in the lower troposphere is a strong Arctic climate forcer responsible for the increase in surface temperature (Flanner, 2013; Sand et al., 2016). In agreement with recommendations by Petzold et al. (2013), the term BC is here used to indicate light absorbing carbonaceous aerosol, while the term equivalent black carbon (or eBC) will indicate BC mass concentration derived from optical measurements. BC impacts the Arctic climate though multiple pathways (Quinn et al., 2011, 2015). In summary, BC contributes to the absorption of solar radiation (direct effect), leading to atmospheric warming, and impacts cloud cover by altering atmospheric convection (semi-direct effect) (Hansen et al., 2005; Bond et al., 2013; Flanner,

2013). In addition, BC can modify cloud lifetime, increase cloud optical thickness and enhance cloud emissivity (i.e. all indirect effects), resulting in warming or cooling of the atmosphere (Albrecht, 1989; Twomey, 1974; Quinn et al., 2008). Finally, once deposited on snow and ice, BC enables more shortwave radiation to be absorbed, increasing warming in a mechanism known as the albedo climate feedback, thus accelerating snow and ice melting in spring (Hansen and Nazarenko, 2004; Flanner et al., 2007; Sand et al., 2013).

In the Arctic, the impact of direct, semi-direct, and indirect effects vary dramatically with season, because solar radiation, cloud properties, and surface reflectivity show large seasonal differences (Quinn et al., 2008; Flanner, 2013; Sand et al., 2013). For this reason, understanding BC seasonal variability is fundamental for a reliable BC climate impact modelling. Nevertheless, ensamble model experiments show that several aerosol models underestimate Arctic BC concentration in the lower troposphere, and often fail in reproducing its seasonality (Koch et al., 2009; Shindell et al., 2008). More recently, models showed a better capability in describing seasonal variability of BC surface concentration, but still under predict cold season averages in North America and Europe by a factor of 2 to 5 (Sand et al., 2013; Quinn et al., 2015; Srivastava and Ravichandran, 2021). Similar discrepancies have been reported by Winiger et al. (2017) simulating surface Siberian Arctic BC with the Flexpart transport model.

The overestimation of BC scavenging in polar regions, where ice-clouds are dominating, has been proposed as one of the factors responsible for BC model underestimation. Browse et al. (2012) enhanced the model ability to describe BC Arctic seasonality by optimising the in-cloud and below cloud scavenging scheme. Zhou et al. (2012) improved the agreement between modelled and observed BC deposition by reducing scavenging in ice and in mixed-phase clouds, but still failed in reproducing the atmospheric concentrations. Lund et al. (2018) observed that reducing the ice-cloud scavenging significantly increased the BC surface concentration in the Arctic, but declined model performance at lower latitudes, highlighting the need of a deeper understanding of processes and properties controlling BC scavenging (Lund et al., 2017).

Model failure in simulating Arctic BC concentration can also be a consequence of the uncertainties of BC emission inventories (Zhou et al., 2012; Sand et al., 2013). For example, a limited number of models include gas flaring emissions (Huang et al., 2015), and their impact remains unclear. In fact, some modelling analysis indicate that gas flaring can account for more than 50% of surface monthly average BC concentration (Stohl et al., 2013; Popovicheva et al., 2022), while radiocarbon measurements suggest an average contribution smaller than 10% (Winiger et al., 2017, 2019). In addition, BC from vegetation fires can account for a significant fraction of BC burden in the Arctic during summer, but emissions show a large spatial and temporal variability (Evangeliou et al., 2016; Winiger et al., 2017, 2016) and depending on their source region, they contribute differently to BC surface concentrations (Stohl, 2006; Stohl et al., 2013; Evangeliou et al., 2016). Both these factors make it challenging to quantify biomass burning impact on the Arctic lower troposphere. Finally, the efficiency of transport mechanisms from the source regions affects Arctic BC variability and burden (Chen et al., 2020; Zhou et al., 2012). Based on a 15-year simulation (1979-1983), Eckhardt et al. (2003) reported that the surface concentration of short-lived pollutants like BC in winter and spring is enhanced by 70% during the positive phase of North Atlantic Oscillation (NAO) index, due to the effective transport from Europe. The analysis of a more recent eBC record in the European Arctic (2001 - 2015) concluded that Scandinavian pattern (SCAN) (Barnston and Livezey, 1987) is a better indicator than NAO, and a negative SCAN phase corre-

sponds to a 35% increase of eBC concentration (Stathopoulos et al., 2021). Several modelling works confirm the relevance of synoptic-scale meteorology to explain BC transport efficiency and its inter-annual concentration variability (Zhou et al., 2012;

60 Chen et al., 2020; Sharma et al., 2013).

Previous studies suggested that local meteorology can be linked to the transport-integrated meteorology (Garrett et al., 2011; Stohl, 2006). For example, Garrett et al. (2011) observed that higher wet scavenging along transport is associated with local temperature around freezing and high relative humidity. Starting from this hypothesis, this paper investigates the link between local meteorological variables and changes of eBC concentration in a European Arctic site, to gain insights into the transport

65 mechanisms of polluted air masses from lower latitudes to the Arctic and the impact of local meteorology. This study aims at a better understanding of local processes and synoptic-scale circulation effect on BC in the Arctic lower troposphere, through the analysis of eBC measurements performed in the Svalbard Archipelago, over a four-year period. First, the manuscript describes the eBC concentration time series and evaluates seasonal differences. Then we assess and discuss the impact of local meteorology and general circulation indices on the observed variability using generalized additive models (GAM). Finally,

70 we analyse the discrepancies between model and observations to identify unaccounted synoptic-scale circulation patterns that could improve the description of eBC temporal variability.

2 Methods

2.1 Measurement site

The measurement site is located at Svalbard (Norway), in the Kongsfjorden region. Aerosol measurements were performed at

75 the Gruvebadet Atmospheric Laboratory (GAL) (78.918° N, 11. 895° E, 61 m asl), located about 1 km south of Ny-Ålesund village, and is part of the Ny-Ålesund Research Station and SIOS network (Svalbard Integrated Observing System) (Song et al., 2021). Meteorological measurements were collected in the Ny-Ålesund village and at the Climate Change Tower (CCT), approximately 1 km from GAL (Mazzola et al., 2016).

Figure 1a shows the location of GAL, Ny-Ålesund village, and the CCT, while Fig. 1b and c report the wind rose during the

80 cold and warm season, respectively. GAL is surrounded by mountain ranges to the south and the west, and by the Kongsfjorden to the north and the east, leading to a wind pattern characterized by higher wind flows from east-southeast, parallel to the fjord direction and blowing from the Kronebreen, Kongsbreen, and Kongsvegen glaciers. A second wind component from south-west is usually characterized by a speed below 4 m s^{-1} , and is due to the wind flow from the Brøggerbreen glacier (Sjöblom et al., 2012; Graßl et al., 2022; Pasquier et al., 2022; Mazzola et al., 2016). The dominant local wind patterns for the cold

85 and the warm seasons are shown in Fig. 1b and 1c, respectively. The winds from direction of Ny-Ålesund village are the least common ones. To minimize the risk of contamination from the village and the harbour, we removed data characterized by a dominant wind direction from 15 to 60 degrees north (corresponding to 3% of the hourly data points).
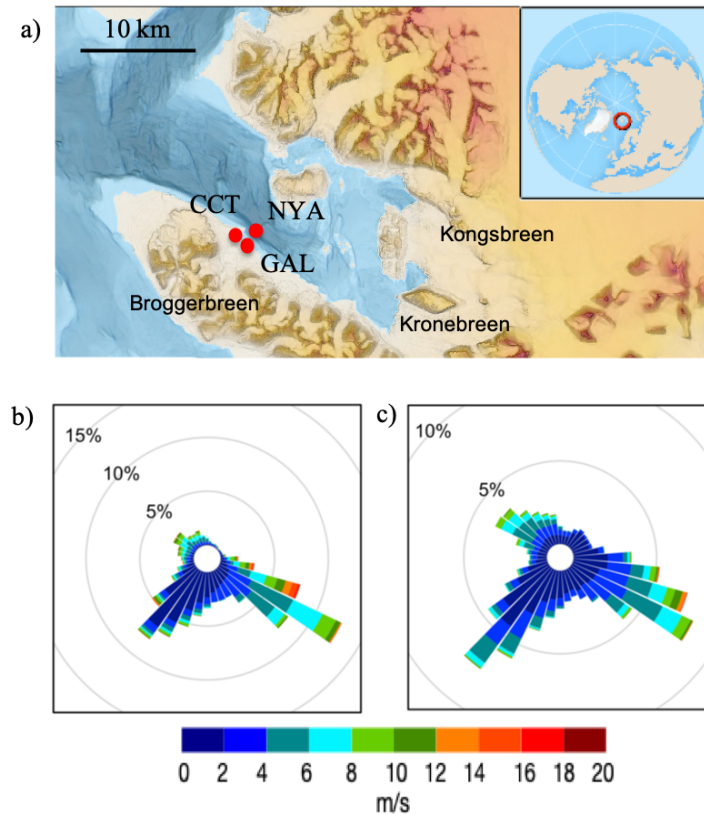
Figure 1. Map of the Kongsfjorden area (a) indicating the position of the Gruvebadet Atmospheric Laboratory (GAL), the Climate Change Tower (CCT), and Ny- Ålesund village (NYA); wind rose for the cold (b) (November - April) and warm (c) (May - October) season derived from wind measurements performed at 2 m from the ground. Map from https://toposvalbard.npolar.no, courtesy of the Norsk Polarinstitutt.

2.2 Aerosol optical properties

Aerosol optical properties have been measured at GAL since 2010, during the warm season, while cold season measurements have been performed routinely only since March 2018. To have a complete description of the seasonal variability, this study focuses on the period 2018 - 2021.

Aerosol particles at GAL were sampled through a Total Suspended Particle (TSP) inlet and the absorption coefficient was measured with a 3-wavelength Particle Soot Absorption Photometer (PSAP, Radiance Research, USA) (Bond et al., 1999) operating at 467, 530, and 660 nm at a nominal flow rate of 1 lpm. Hourly absorption data were calculated from measurements with a 4 s time resolution, and corrected for spot size and flow rate according to Bond et al. (1999) and Ogren (2010). We discarded measurements characterized by transmittance values lower than 0.5. Finally, absorption coefficients data were corrected for filter loading and scattering artefacts according to Virkkula (2010).

We measured the scattering coefficients with a nephelometer (M903, Radiance Research, USA) at 530 nm, and corrected for illumination and truncation error according to Müller et al. (2009). Scattering coefficients at 467 and 660 nm were derived assuming a scattering Ångström exponent of 1.15 (Schmeisser et al., 2018). Absorption and scattering coefficients were adjusted to standard temperature and pressure.

From October 2019 to October 2020, a Multi Angle Absorption Photometer (MAAP, Magee Scientific Corporation) measured aerosol absorption coefficient at 637 nm at GAL, in parallel with the PSAP, to validate the PSAP correction algorithm. The MAAP worked at 1-minute time resolution and data were averaged over one hour. MAAP absorption coefficients were corrected according to Müller et al. (2011) and then adjusted to 660 nm to be compared with PSAP measurements, assuming an absorption Ångström exponent of 1.

2.3 Meteorological data

Meteorological measurements (temperature, pressure, relative humidity, radiation, wind direction, and wind speed) were continuously performed at the Climate Change Tower (CCT at about 1 km from GAL) at 1-minute time resolution, while we used hourly precipitation, 3-hourly cloud cover, and cloud cover height measured at the Ny-Ålesund station of the Norsk Klima Service Center (https://klimaservicesenter.no, last visited in June 2022). Daily averages were calculated for all the variables, other than precipitation, for which daily cumulative values were instead derived from hourly data.

We obtained boundary layer height (BLH) at GAL and sea level pressure maps in the northern hemisphere from hourly ECMWF reanalysis ERA5 data (Hersbach et al., 2020) at a spatial resolution of $0.25° \times 0.25°$ (https://cds.climate.copernicus.eu/ last visited in January 2023).

General circulation indices (North Atlantic Oscillation NAO, Arctic Oscillation AO, Scandinavia index SCAN) were downloaded from the NOAA Climate Prediction centre (https://www.cpc.ncep.noaa.gov, last visited in June 2022) at daily (NAO and AO) and monthly (SCAN) time resolution. The NAO is a measure of the difference in sea-level atmospheric pressure between the Icelandic Low and the Azores High (Hurrell, 1995). Positive NAO index is associated with low pressure at high latitudes of the North Atlantic and potential transport of polluted air masses from lower latitudes (Eckhardt et al., 2003). The AO represents the strength of winds circulating around the North Pole, which are able to isolate cold air masses to the high latitudes. Low AO index indicates weaker winds, which allow the potential intrusion of warm air masses from lower latitudes. SCAN index is based on the analysis of 700 hPa geopotential height patterns and is associated to a strong center over Scandinavia and two weaker centres with opposite signs over western Mongolia and Eastern Russia (Barnston and Livezey, 1987). Stathopoulos et al. (2021) observed that negative SCAN phase was associated with higher eBC concentration at the Zeppelin Observatory (Svalbard).

Daily Greenland Blocking Index (GBI) was downloaded from the Global Climate Observing System webpage (https://psl.noaa.gov/gcos_wgsp/, last visited in June 2022). GBI is the mean 500 hPa geopotential height over the region that extends from 60° - 80° N and 20° - 80° W, and measures the blocking pattern over Greenland.

To investigate below cloud and in-cloud scavenging during transport to the Arctic, we downloaded daily maps of precipitation rate from the Copernicus Climate change service (https://cds.climate.copernicus.eu/#!/home last visited January 2023). Daily

maps (1° x 1° horizontal resolution) were derived from satellite observations within the Global Precipitation Climatology Project (GPCP).

2.4 Back trajectory analysis

135 7-day LAGRANTO back trajectories were calculated every 6 hours from March 2018 to December 2021, initialized at 10 and 30 hPa above ground level at GAL (Sprenger and Wernli, 2015; Wernli, 1997). Modelling data suggest that BC atmospheric lifetime is on average 5.5 days ($\pm$2 days) (Szopa et al., 2021). Similarly, Backman et al. (2021) estimated that BC emissions affecting Arctic surface observatories can travel in the atmosphere for up to 7 days prior to reaching the receptor site (Backman et al., 2021). 7-day duration was selected to capture BC atmospheric lifetime, as well as removal processes along trajectories

140 (Cremer et al., 2022; Evangeliou et al., 2016). The trajectory calculator used ERA5 as input meteorology, with a horizontal resolution of 0.5° x 0.5° and vertical resolution of 137 levels up to 1 hPa. We then reconstructed the probability residence time maps (Ashbaugh et al., 1985) to a resolution of 1°x1° (Fig. S1) to compare with BC emission maps and precipitation rate maps.

2.5 Generalized Additive Model

145 We used Generalized Additive Models (GAMs) to investigate the impact of local meteorology and synoptic-scale circulation on the eBC variability. GAMs do not assume a linear relationship between variables (Hastie and Tibshirani, 1986); instead this method describes the relationship between each predictor and the dependent variable (in this case eBC concentration) as a smooth function, generally non-parametric. The different smooth functions can be determined simultaneously, and the dependent variable is then described as a linear combination of the smooth functions, each depending on a single predictor.

150 GAMs have been successfully employed in previous studies to investigate the dependency of particulate matter and particle number concentration on meteorological variables in urban and remote locations (Barmpadimos et al., 2012, 2011; Clifford et al., 2011; Crawford et al., 2016). In such studies, a logarithm transformation was applied to the pollutant concentration to obtain an approximate normal distribution of the dependent variable and improve model residual interpretation (Barmpadimos et al., 2011).

155 We built two different GAMs to describe eBC concentration observed during the cold (November - April) and the warm (May - October) periods, assuming that different mechanisms might control pollution variability. This assumption is corroborated by the fact that eBC observed at Zeppelin (at about 1 km from GAL) is characterized by significantly different source regions during the warm and cold season, as defined above (Stathopoulos et al., 2021; Eleftheriadis et al., 2009). Furthermore, Stathopoulos et al. (2021) highlights that large scale circulation patterns that impact the pollutant transport from lower lati-

160 tudes (NAO, OA, and SCAN) shows opposite behaviours during these two periods of the year. In addition, we analysed daily rather than hourly eBC concentrations, to increase eBC signal-to-noise level and to include in the analysis covariates with time resolution coarser than 1 hour, such as general circulation indices. Finally, mild and extreme outliers were removed using the interquartile range criteria (2 out of 1026 daily data points were removed).

The logarithm of eBC concentration was modelled according to the following equation:

$$ln(eBC) = \sum_{j=1}^{p} s_j(x_j) + \sum_{j=p+1}^{q} \beta_j x_j + a + \varepsilon \qquad (1)$$

where s_j is the smooth function describing the j-th predictor, β_j is the linear coefficient of categorical variable x_j, p is the number of continuous variables, (q-p) is the number of categorical variables, a is the intercept and ε is the residual.

We implemented GAM analysis using the mgcv R package (Wood, 2017). We choose penalized thin plate splines as base splines to define the smooth functions s_j, while the smoothing parameters were estimated using the REML algorithm (restricted maximum likelihood), to reduce the risk of data over-fitting. Circulation indices and meteorological parameters were tested as continuous variables. We also tested precipitation and wind direction as categorical variables. In addition, we included day of the year (DOY) and truncated Julian Day (tJul or continuous day count from May 24, 1968) among the investigated variables to take into account all processes that could not be explained by local meteorological variables or circulation indices, such as seasonal and annual variability of emissions and removal processes during transport. DOY ranged between 1 and 366, while Jul varied between 18178 and 19579.

2.6 Model definition

To build the seasonal GAMs, we first selected those variables able to explain the largest eBC variability using an iterative approach as described by Jackson et al. (2009) and illustrated in the following steps:

Step 1. Univariate GAMs were created using the explanatory variables, one at a time, and the variable associated to the largest deviance explained was selected. The deviance explained is the fraction of variance of eBC data described by the model.

Step 2. The remaining variables were added to the GAM defined in step 1, one at a time, and the deviance explained was re-calculated. The model characterized by the highest deviance explained was chosen.

Step 3. Variable selected in step 1 was removed and replaced by the remaining variables. If the new deviance explained was higher than the one from step 2, the new model was retained. If two variables were associated to a similar increase of the deviance explained, the one characterized by higher significance (i.e. lower p-value) was selected.

Step 4. To test the model robustness, we verified that all the variables included in the model were significant at least at 95% significance level.

Step 5. Multi-collinearity of GAM covariates should be avoided, as it would make it difficult to discriminate the impact of the different variables and would introduce redundancy in the model. To test multi-collinearity, when a new variable was added to the model, the Variance Inflation Factor (VIF) was calculated as follows:

$$VIF = \frac{1}{1-r^2} \qquad (2)$$

r is the Pearson's correlation coefficient that defines the correlation of the last added variable against all the other variables already included in the multivariate GAM (Barmpadimos et al., 2011). As a general rule, VIF equal to 1 corresponds to no

correlation, while VIF between 1 and 5 indicate a weak correlation. In this study, if the VIF exceeded 2.5, the variable was not added to the model and the covariate with the second highest deviance explained was tested. A VIF equal to 2.5 was chosen because it corresponds to a coefficient of determination of 0.6, which is the maximum collinearity among covariates that was considered acceptable.

Step 6. We repeated step 2 to 5 until the deviance explained increase was smaller than 2%.

Finally, we tested normality (normal distribution of the residuals around zero), homoscedasticity (constant variance of the residuals), and linearity (linear correlation of the predicted versus observed values) of the model results.

2.7 BC emissions

We derived BC monthly emissions from anthropogenic sources using the EDGARv5.0 global emission database (https://edgar.jrc.ec.europa.eu/index.php/dataset_ap61, last visited July 2022) developed by the Joint Research Center of the European Commission (Crippa et al., 2019). Monthly gridded emissions for different activity sectors are available for the years 1970 - 2018 at a spatial resolution of $0.1° \times 0.1°$. We used the most recent data, i.e., 2018 emissions, as representative for the period 2018-2021. The following emission sectors were considered: power industry, refineries and transformation industry, combustion for manufacturing, residential combustion, road transportation, other transportation, and shipping. These sectors, together with agricultural burning, account from more than 94% of total BC emissions in Europe, Russia, Canada, and USA, excluding Land Use, Land Use Change and Forestry (LULUCF) sector (Fig. S2).

The EDGAR inventory does not include the contribution from LULUCF, thus we derived BC monthly emissions from open burning, including agricultural waste burning, using the Global Fire Emission Database GFED (https://www.globalfiredata.org last visited January 2022). GFED is based on fire activity and vegetation property data from satellite observations (Giglio et al., 2013). We employed GFED4s version, which includes also small fires (Randerson et al., 2012; van der Werf et al., 2017). For each grid cell with spatial resolution $0.25° \times 0.25°$, we calculated BC emissions by multiplying the total dried matter emissions (in kg m^{-2} month^{-1}) by the grid cell area (m^2) and by the BC emission factors (g of BC per kg of dried matter) of the six different BC sources included the database: savanna, grassland and shrubland fires, boreal forest fires, temperate forest fires, tropical deforestation and degradation, peat fires, and agricultural waste burning (Akagi et al., 2011; Andreae and Merlet, 2001).

To select the regions that contributed to the eBC measured on Svalbard, we overlapped the monthly emission maps from EDGAR and GFED to the back trajectory residence time maps calculated for the corresponding month from the LAGRANTO analysis tool.

3 Results and discussion

3.1 PSAP data validation

225 Equivalent black carbon (eBC) is derived from the aerosol absorption coefficient (B_{abs}) measured by a PSAP, whose measurements were corrected for filter loading and light scattering induced by particles deposited on the collection filter. Correction algorithm, developed by Virkkula (2010), is here validated by comparing hourly PSAP data with co-located MAAP measurements during one year, from October 2019 to October 2020. MAAP is employed as a reference technique since it automatically corrects aerosol absorption coefficient for filter loading and scattering by measuring, in addition to light attenuation, the

230 backscattering of particles on the filter (Müller et al., 2011; Petzold and Schönlinner, 2004).

Figure 2 compares the time series of hourly PSAP and MAAP absorption coefficients at 660 nm. During the inter-comparison period the absorption coefficient ranged between the detection limit (0.013 Mm^{-1} for MAAP and 0.002 Mm^{-1} for PSAP) (Asmi et al., 2021) and 2.8 Mm^{-1}, with an average value of 0.22 Mm^{-1}. PSAP agrees well with the MAAP data, with a Pearson's coefficient of 0.93. The linear fit is characterized by a slope equal to 0.982 ($\pm$0.005) and an intercept of 0.042

235 ($\pm$0.002). The relationship between the two time-series is comparable to the one reported by Asmi et al. (2021) during an inter-comparison field experiment in northern Finland, with absorption coefficient values similar to those observed during this study. The agreement between MAAP and PSAP time series corroborate the suitability of the correction algorithm described in section 2.2 (Virkkula, 2010).

3.2 eBC seasonality

240 eBC was then derived from the absorption coefficient time series at 660 nm, assuming a constant Mass Absorption Cross section (MAC) equal to 10.2 m^2 g^{-1}, in agreement with the MAC calculated by Ohata et al. (2021) with instrument techniques similar the to ones employed in this study (See section S1 and Table S1)

Figure 3 shows the monthly variability of eBC concentrations from 2018 to 2021. Only months characterized by a hourly time temporal coverage larger than 50% are reported, to guarantee data representativeness (Rose et al., 2021). eBC concentration

245 averaged 22 ng m^{-3} ($\pm$20 ng m^{-3}) during the cold season (November - April) and 11 ng m^{-3} ($\pm$11 ng m^{-3}) during the warm season (May - October). The highest eBC monthly averages were observed from January to April, corresponding to the Arctic Haze period, while the lowest were recorded between June and October. The observed eBC seasonality agrees with previous studies from Svalbard (Eleftheriadis et al., 2009; Stathopoulos et al., 2021). The average eBC concentration measured at the Zeppelin Observatory, at about 1 km from GAL and at 474 m altitude, averaged 21 ng m^{-3} and 7 ng m^{-3} in the cold

250 and warm season, respectively, in the period 2011-2015 (Stathopoulos et al., 2021). Higher seasonal averages were instead reported in previous years (Eleftheriadis et al., 2009), in agreement with a decrease of BC concentrations in the Arctic during the last three decades (Schmale et al., 2022). Increased vertical mixing in the lower troposphere and more frequent precipitation during summer promote aerosol dilution and removal processes in the warmer period, leading to a reduction of the surface eBC concentration (Stohl, 2006; Garrett et al., 2011). Furthermore, the extension of the Arctic front towards lower latitudes during
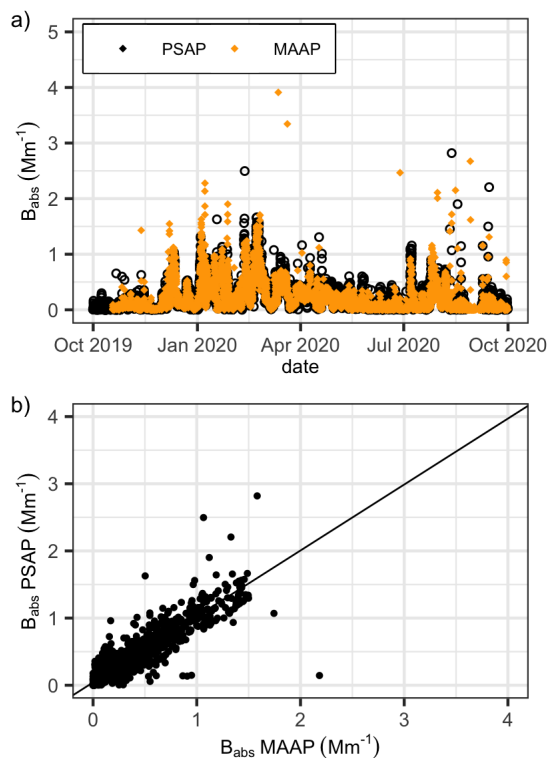
Figure 2. Time series of aerosol absorption coefficient at 660 nm (B_{abs}) measured by a Particle Soot Absorption Photometer (PSAP in black) and a Multi Angle Absorption Photometer (MAAP in orange) at Gruvebadet (panel a), and comparison of B_{abs} measured by the two instruments during the inter-comparison experiment, from October 2019 till October 2020 (panel b).

the cold period facilitates the transport of polluted air masses from populated regions in northern Europe and Russia (Quinn et al., 2015; Stohl, 2006).

Figure 3 shows some variability of the eBC monthly statistics from one year to the other. Statistically significant differences were observed mainly during the cold and the transition periods. In 2018, March and May showed significantly lower eBC concentrations compared to the same months of the other investigated years, while in 2020, February and October were characterized by slightly larger concentrations. January and November 2021 exhibited lower and higher eBC values relative to the other monthly means, respectively. During the warm period, the largest difference was observed in July 2020, when mean eBC concentration was higher compared to the same months of the remaining analyzed years.

3.3 Analysis of drivers controlling eBC variability

In this section we use GAMs to identify and discuss the explanatory variables that best describe the variability of eBC in the European Arctic and understand how they link to the synoptic-scale circulation and local meteorology.
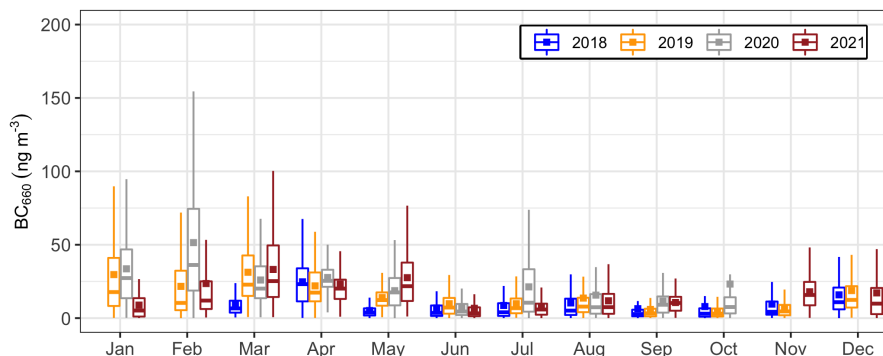
Figure 3. Box-whisker plot of equivalent Black Carbon concentration (eBC) according to months and years. Lower and upper box boundaries correspond to 25th and 75th percentiles, respectively, vertical lines extend to the minimum and the maximum without outliers, horizontal lines inside the box indicate the medians, while squares correspond to the averages.

To facilitate the interpretation of the covariates effect, we first investigated the correlation among them. Figure S3 reports the Pearson's correlation matrices for the cold and warm period. Wind speed correlated with boundary layer height, because local wind promoted atmospheric vertical instability. As expected, NAO and AO correlated with each other and anticorrelated with GBI, since they describe opposite pressure fields (Hanna et al., 2014). During the cold season, atmospheric pressure
270 correlated with GBI and anticorrelated with AO, because a positive GBI phase and negative AO phase are characterized by a high pressure system over the Arctic region. The correlation weakened in the warm season due to the lower variability of GBI and AO indices.

3.3.1 Cold season

Table 1 reports the covariates selected for the cold season GAM, together with the deviance explained by the model after the
275 addition of each variable, and the corresponding p-values. Low p-values indicate high significance of the relationship between ln(eBC) and the explanatory variable.The smoothed functions describing the dependency of the eBC on each covariate are shown in Fig. 4. In each box, the vertical axis shows the additive effect of one specific covariate on the eBC concentration, as a function of the covariate values, reported on the horizontal axis.

The first variable selected for the definition of the cold season GAM was truncated Julian Day (tJul), which alone accounted
280 for 19% of the eBC variance (Fig. 4a). Although DOY was the second variable with the highest deviance explained in the univariate models (16%), it was not selected as explanatory variable during the multivariate model definition (section 2.6), indicating that truncated Julian Day already accounted for the seasonal variability that would have been described by the DOY. To clarify the impact of truncated Julian Day, Fig. 5a reports the monthly average of eBC concentration derived by the GAM model using this covariate alone. Truncated Julian Day combines the effects of drivers that are characterized by a
285 clear seasonal and inter-annual variability. On average, modelled eBC concentrations were similar in November and December

Table 1. Explanatory variables of cold season and warm season GAM. The order of the variables corresponds to the selection order during the GAM model definition. Deviance explained is the cumulative value of each variable and the preceding ones, while the p-values are indicative of each variable statistical significance (for all variables larger than 99.9%).

Cold season	Dev. explained	p-value
Truncated Julian Day (tJul)	0.19	$<2 \ 10^{-16}$
Pressure (press)	0.29	$3.87 \ 10^{-5}$
Temperature (temp)	0.35	$1.91 \ 10^{-6}$
BLH	0.40	$<2.0 \ 10^{-16}$
GBI	0.44	$7.74 \ 10^{-5}$
Relative humidity (RH)	0.47	$2.84 \ 10^{-4}$
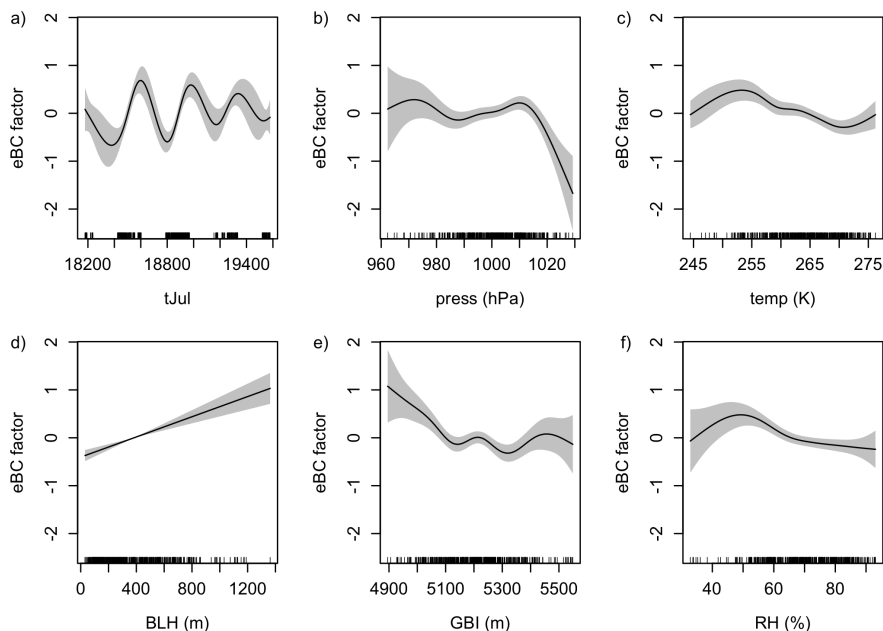
Figure 4. Smooth functions of the variables contributing to define eBC concentration in the cold season GAM. In each plot, the y-axis reports the change of the eBC concentration relative to the seasonal average; an eBC factor equal to +1 corresponds to an increase in eBC concentration equal to 100% relative to the cold season average. The tick marks on the x-axis show the distribution of the predictor values across their variability ranges.

and increased by a factor of two from November to April, with some interannual differences. Previous studies attributed BC seasonal variability to the increase of wet scavenging efficiency in the colder months (Arctic Haze) and the retreat of the Arctic front during the warmer months, the latter reducing the source regions potentially able to impact the Arctic air quality (Stohl,
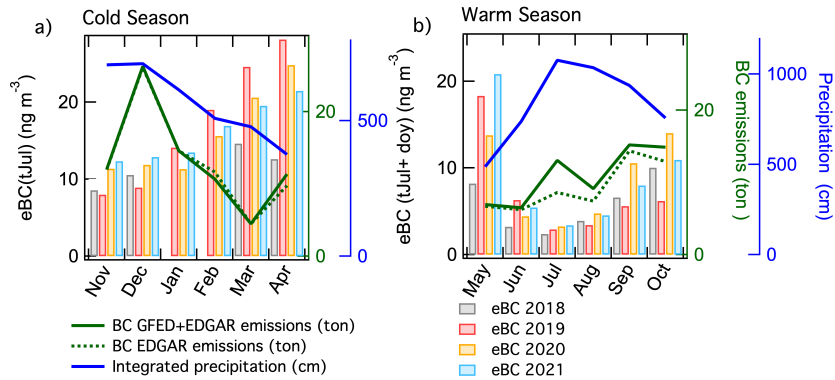
Figure 5. eBC concentration predicted by truncated Julian Day in the cold season (panel a) and by truncated Julian Day together with DOY in the warm season (panel b); the blue lines indicate the monthly precipitation integrated along back trajectories, while the green lines correspond to BC emissions monthly averages excluding (dotted lines) and including (continuous lines) open burning emissions.

2006; Garrett et al., 2011; Freud et al., 2017). To investigate the relative significance of these two effects, Fig. 5a reports the
290   monthly precipitation and BC emissions integrated along trajectories. BC monthly emissions were calculated by multiplying the back trajectory residence time maps from LAGRANTO analysis by the BC emission flux maps, and thus they take into account the Arctic front seasonal variability. BC emissions did not explain the model eBC trend, in fact they increased from November to December, and then decreased progressively during the following months. Instead, the integrated precipitation were comparable in November and December, and then decreased progressively from December to April, showing an opposite
295   trend compared to the eBC predicted values. Monthly averages of eBC derived from truncated Julian Day weakly anticorrelated with the precipitation rate along back trajectories (r = -0.43), whilst the predicted eBC showed no link with BC emission variability (r = -0.11) (Fig. S4), indicating that scavenging efficiency had a stronger impact on eBC seasonality than emission variability. The anticorrelation (negative r value) indicate that an increase in precipitation rate was associated with a decrease in surface eBC concentration, as expected due to wet scavenging.

300   The second selected covariate was surface atmospheric pressure, which explained 29% of the eBC variance in combination with truncated Julian Day (Fig. 4b). Statistically significant effects were observed for pressure above 1010 hPa. In particular, when pressure increased from 1010 to 1025 hPa, eBC decreased by 70%. The threshold values of 1010 hPa is relatively high when compared to the average surface pressure recorded during the cold season (1000 hPa) and the average values reported for the same location in previous years (about 1006 hPa) (Maturilli et al., 2013; Mazzola et al., 2016). Figure S5 reports the
305   average sea level pressure (SLP) maps derived from ERA5 re-analysis, and corresponding to the periods characterized by pressure at GAL higher than 1010 hPa and the entire cold season. In the first case, the SLP over the Arctic was higher than the average, and a centre of high pressure was localized over Svalbard. The difference in local SLP corresponds to substantially different synoptic-scale SLP patterns, and hence local pressure can be considered as a proxy for large-scale synoptic circulation. High pressure patterns over the Arctic in winter weakens westerly flows over the Atlantic Ocean and prevents the advection
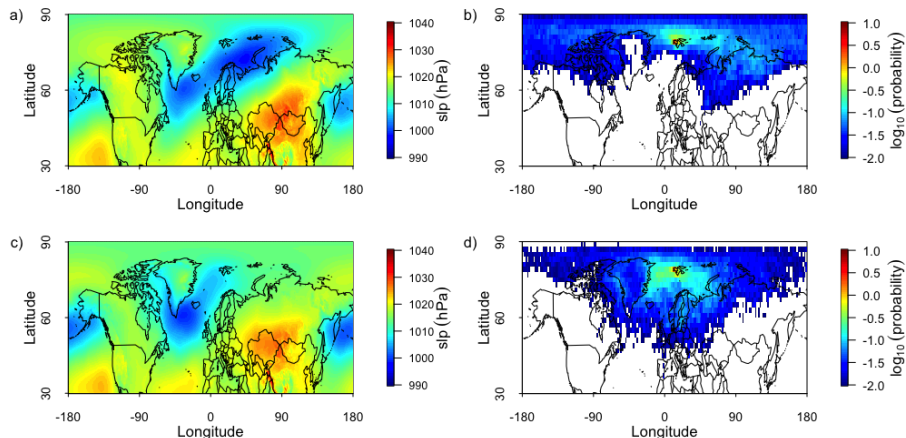
Figure 6. Average sea level pressure map and residence time probability map when temperature at GAL was lower than 265 K (panel a and b, respectively) and higher than 265 K (panel c and d, respectively) during the cold season. Residence time probability maps are based on 7-day back trajectories.

310 of air masses from the European continent to the higher latitudes (Maturilli and Kayser, 2017). Thus, the reduction of eBC concentration at high surface pressure observed in this study is explained by a blocking of pollution transport from lower latitudes.

The third selected variable was surface temperature, explaining 35% of the eBC variance, in combination with truncated Julian Day and surface pressure (Fig. 4c). A significant impact of this covariate was observed at values between 255 K and 270 315 K (corresponding to 75% of data points), when 10 K temperature raise led to a drop of eBC concentration by 32%, on average. Increase of temperature corresponds to the transport of warmer and more humid air masses to Svalbard (Maturilli and Kayser, 2017; You et al., 2022). The cold season mean specific humidity was 1.5 g kg^{-1} , while it averaged 2.2 g kg^{-1} when the temperature was higher than 265 K. The relative increase in specific humidity suggests that air masses reached Svalbard after spending most of the time over the ocean, rather than over the continental areas, where most of the emissions originate. Figures 320 6a and c compare the average sea level pressure over the Northern Hemisphere and the residence time of back trajectories reaching GAL when local temperature was lower or higher than 265 K. Under colder conditions, a strong pressure gradient between Siberia and the Eurasian Arctic supported the transport of air masses from the northern Siberia to higher latitudes, favouring the transport of air pollutants to Svalbard. Conversely, when temperature at GAL was relatively higher, the Siberian anticyclone weakened while the pressure over the European Arctic increased, blocking the transport of air masses from the 325 polluted European and Asian mainland, while favouring the transport from the Atlantic Ocean sector. Figures 6b and d report the probability residence time maps corresponding to the two conditions and clearly shows that when the temperature at GAL was higher, air masses spent more time over the Fram Strait; this led to a decrease in the observed eBC concentration.

Boundary layer height (BLH) increased the deviance explained by the GAM up to 40% (Fig. 4d). The effect of this covariate was particularly significant when BLH was shallow (below 600 m). In fact, eBC increased by about 40% when BLH increased

from 100 m up to 600 m. Rader et al. (2021) observed that anthropogenic aerosol is transported great distances towards the European Arctic in the lower free troposphere, and then it might mix down in the boundary layer in areas with complex orography, such as Ny-Ålesund in Svalbard. It follows that a higher boundary layer favours the downward mixing of BC from the free troposphere, increasing the observed concentrations at sea level. Furthermore, in the cold season shallow boundary layer conditions at GAL were dominated by very weak flow from south-west, while increasing BLH was associated to the shift of prevailing wind direction towards east-southeast and increasing wind speed (Fig. S6 a-d). Winds from east-southeast corresponds to the descending movements of air masses along the slope of the glaciers at the western edge of the Kongsfjord, promoted by sea-breeze and terrain orography (Sjöblom et al., 2012). It is likely that such descending air masses contributed to the transport of pollutants from the lower free troposphere towards GAL.

GBI and RH, the two remaining variables included in the cold season GAM, increased the deviance explained by the model up to 47% and had a small effect on the eBC level (Fig. 4e and 4f, respectively). eBC concentration increased when GBI was smaller than 5100 m (Fig. 4e), due to the weakening of the blocking system triggered by the high pressure over Greenland (Dekhtyareva et al., 2022). The effect of relative humidity above 50% was a slight reduction of eBC concentration, likely due to the local in-cloud and below-cloud scavenging (Fig. 4f). When relative humidity was lower than 50%, the effect on eBC was characterized by a large uncertainty due to the small number of data points in this humidity range.

3.3.2 Warm season

Table 2 shows the covariates selected for the warm season GAM (May - October), while Fig. 7 reports the smoothed functions describing the link between eBC and the selected covariates.

Table 2. As in Table 1, but for the warm season. The p-values are indicative of each variable statistical significance (** corresponds to significance larger than 99.9% and * larger than 95%).

Warm season	Dev. explained	p-value
Truncated Julian Day (tJul)	0.13	$<2\ 10^{-16}$ **
Day of the Year (DOY)	0.22	$<2\ 10^{-16}$ **
Temperature (temp)	0.32	$<2\ 10^{-16}$ **
Relative humidity (RH)	0.36	$7.21\ 10^{-5}$ **
Radiation (Rad)	0.40	$4.59\ 10^{-2}$ *
BLH	0.43	$3.45\ 10^{-5}$ **
AO	0.46	$1.38\ 10^{-2}$ *

The first two selected covariates were truncated Julian Day and DOY, which together explained 22% of the eBC variance (Fig. 7a and 7b, respectively). We discuss them together as they describe processes characterized by a smooth interannual and seasonal variability. The selection of both truncated Julian Day and DOY as explanatory variables indicates larger interannual
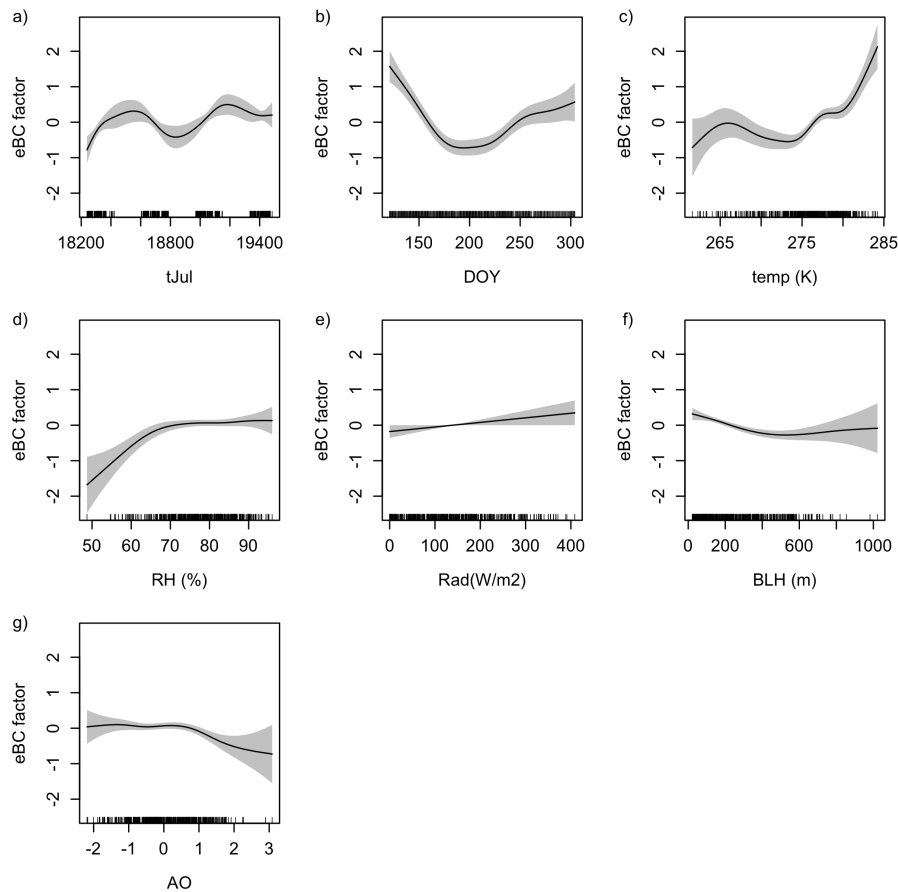
Figure 7. Smooth functions of the variables contributing to define eBC concentration in the warm season GAM.

differences in the seasonal trends compared to what was observed during the cold season, when the selection of truncated Julian Day excluded DOY from the model. Figure 5b reports the modelled eBC concentration derived from DOY and truncated Julian Day. The monthly modelled eBC averages show minimum values in July and then increase during the following months with different rates during the different years. On average, estimates of eBC concentrations decreased by 80% from May to July and

355 then increased from July to October by 53% to 77%. The seasonal variability of BC emissions is not linked to the modelled eBC (Fig. 5b). Conversely, precipitation integrated along back trajectories increased by a factor of two from May to July and then decreased till the end of summer, mirroring the trend of modelled eBC. Monthly averages of modelled eBC clearly anticorrelated with precipitation (r = -0.70), indicating that eBC variability was strongly affected by the efficiency of removal processes during transport. This was particularly evident in the warm season, which showed higher precipitation values than

360 the cold season (Fig. S4). The correlation with monthly emissions was instead negligible (R= -0.13).

The third selected variable was temperature, which together with truncated Julian Day and DOY explained 32% of the eBC variance (Fig. 7c). Statistically significant effects were observed for temperatures above 275K, when eBC increased by
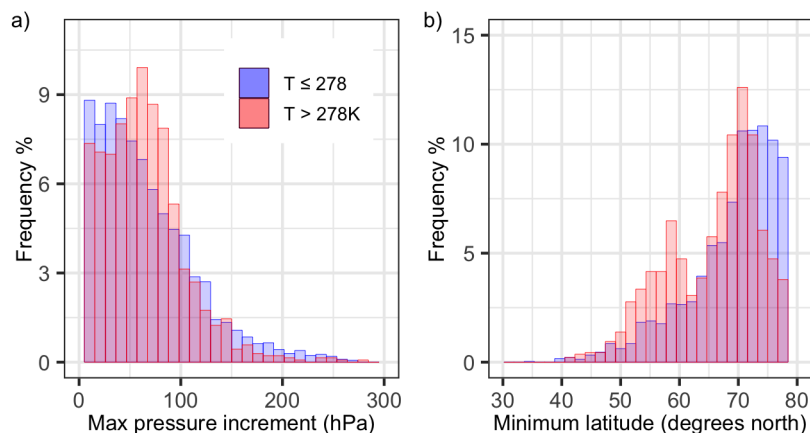
Figure 8. Histograms reporting the frequency of back trajectory maximum pressure increase during the last 48 hour before reaching GAL (panel a) and minimum latitude reached during the seven days before reaching the observatory (panel b). Back trajectory data of colder days are reported in blue, warmer days in red, while purple area corresponds to the overlapping region of the two histograms.

about 88% when temperature increased by 10 K. Higher temperature in the Arctic could be due to diabatic warming, adiabatic warming due to subsidence, or intrusion of air masses form lower latitudes (Papritz, 2020). The analysis of meteorological
365 parameters during transport shows that only a limited number of back trajectories arriving at GAL during warmer days (average temperature higher than 278 K) experienced diabatic warming before arriving at the observatory (10%). Furthermore, we investigated adiabatic warming due to subsidence based on the maximum pressure increase experienced by the back trajectories during the last 2 days before reaching GAL (Binder et al., 2017). The frequency distribution of maximum pressure rise in Fig. 8a shows a slightly higher frequency of back trajectories undergoing a pressure increment between 50 and 100 hPa in warmer days
370 compared to colder days. The pressure change indicates the subsidence from the lower free troposphere just before reaching the observatory. Finally, to study the intrusion of air masses from lower latitudes, the histograms in Fig. 8b reports the frequency distribution of the minimum latitudes reached by the back trajectories up to 7 days before arriving at GAL, as a function of the average daily temperature. The histogram comparison indicates that it was more likely that air masses originated from regions south of the 70th parallel during warmer (62% of the time) than colder days (40% of the time). To further validate these results,
375 Fig.S7a and c show the average sea level pressure while Fig.S7b and c report the residence time maps corresponding to 7-day back trajectories reaching GAL during the warm season. Colder temperatures (T < 278 K, 69% of the time) at the observatory corresponded to the arrival of air masses that spent more time over the Arctic Ocean and Greenland coasts (Fig. S7e). On the other side, warmer temperature periods (T>278 K, 31% of the time) were characterized by a lower pressure system over the north Atlantic Ocean that favoured the transport of air masses from lower latitudes and through northern Europe and Russia
380 (Fig. S7e). To summarize, the higher eBC concentrations observed at GAL during warmer days can be due to the effective transport of polluted air masses from lower latitudes, as well as to the intrusion of pollution from the lower free troposphere.

RH was selected at the fourth step, and increased the model deviance explained up to 36% (Fig. 7d). Dry conditions at GAL (RH below 70%) corresponded to a reduction in eBC concentration by about 30%. No effect was observed for larger RH. The average specific humidity was 2.5 ± 1.1 g kg^{-1} and 3.9 ± 1.0 g kg^{-1} when RH was lower and higher than 70%, respectively. Figure S8 reports the analysis of specific humidity and pressure along back trajectories arriving at GAL under dry and wet conditions. In both cases, specific humidity progressively increased along the trajectories, indicating that wet scavenging could not explain the lower eBC concentrations observed in drier days. Conversely, low RH at GAL corresponded to the arrival of air masses that spent most of their time at higher altitudes compared to air masses arriving under wetter conditions. Likely, air masses moving at higher altitudes could not collect water and pollutants from the surface of ocean and land, and resulted in lower specific humidity and lower eBC concentration at GAL.

The next variable included in the warm season GAM was radiation (Fig. 7e), which brought the model deviance explained to 40%. eBC concentration raised by 23% when radiation increased from 50 W m^{-2} to more than 100 W m^{-2}, likely due to the decreased probability of aerosol scavenging from low-level clouds and drizzle. This is confirmed by the reduction of the radiation impact when cloud height was added to the model as a factor covariate. In particular, the effect of low-level clouds (clouds below 500 m) in the warm period was a reduction of eBC concentration by 23%, on average. Low-level clouds are usually associated with rain and drizzle, with the latter one not well captured by cumulative hourly precipitation measurements (Nystuen, 1999).

The last covariates added to the model were BLH and AO, (Fig 7f and 7g, respectively) which brought the deviance explained up to 46%. The warm season BLH had an opposite effect compared to the one observed in the cold season. In fact, when BLH decreased from 400 m to less than 100 m, the eBC concentration increased by about 60% (Fig. 7f). The effect of BLH is likely controlled by the dominating wind circulation during shallow boundary layer conditions (Fig. S6 e-g). When BLH was lower than 100 m, circulation was mainly characterized by winds from east and east-southeast. This wind pattern was triggered by air masses descending along the slope of the glaciers at the western edge of the Kongsfjord (Sjöblom et al., 2012), which promoted the transport of pollutants form higher altitudes and their intrusion in the shallow boundary layer (Graßl et al., 2022). Furthermore, the weak wind speed favoured eBC accumulation. Days with BLH between 100 m and 400 m were instead characterized by progressively higher wind speed and more frequent winds from southwest (from the Brøggerbreen glacier) and northeast (from the entrance of the fjord). Likely, the lower altitude of the mountain ridge to the southwest compared to western edge of the fjord did not allow an affective transport of pollutants from the lower free troposphere. Similarly, the entrance of air masses from the ocean direction at sustained wind speed (2 to 8 m s^{-1}) contributed to pollutant dispersion. Finally, for BLH larger than 400 m, the model uncertainty increases and effect of BLH became less clear.

The effect of AO (Fig. 7g) goes in the same direction of the NAO impact observed at Zeppelin during the warm season, with higher eBC during AO (or NAO) negative phase (Stathopoulos et al., 2021). Negative AO phase corresponds to weaker polar winds and potential intrusion of polluted air masses from lower latitudes. In addition, Christoudias et al. (2012) reported that positive NAO phase is associated with increased precipitations over northern Europe. Since NAO and AO phases correlated during the investigated period, the reduction of eBC during high AO periods could also be attributed to the enhanced BC scavenging during transport to the Arctic.
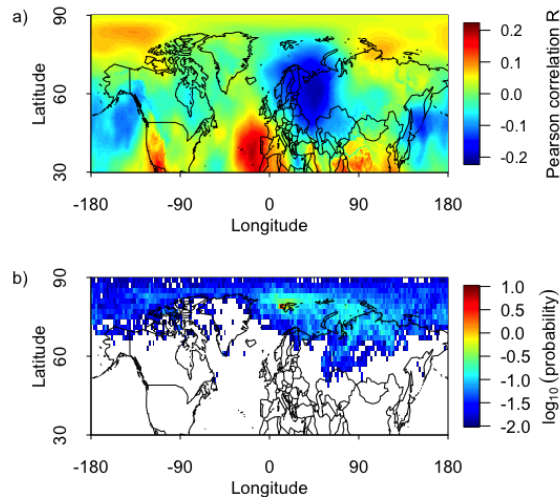
Figure 9. Correlation map of SLP anomalies during the cold period and GAM model residuals during the same season (panel a); Residence time probability map for 7-day back trajectories when the pressure gradient between western Russia and the Atlantic Ocean was larger than 20 hPa (panel b).

3.4 Unaccounted synoptic scale circulation patterns and model performance

Stathopoulos et al. (2021) observed that eBC variability at the Zeppelin Observatory (Svalbard), at about 1 km from GAL, was affected by the Scandinavian index (SCAN). SCAN is a measure of the pressure difference between northern and southern

420 Europe and a positive index indicates a blocking activity over Scandinavia and western Siberia. Negative SCAN values are generally associated to higher eBC concentration at Svalbard, due to favourable pollution transport from northern Eurasia, especially in the cold period (Stathopoulos et al., 2021). The effect was less clear during the warm season, although the authors reported a link between negative SCAN phase and high eBC concentration during the most recent years (Stathopoulos et al., 2021). Since SCAN was available at monthly time resolution, it was not included in the GAM definition, but we investigated

425 its effect on monthly eBC concentrations and model biases. During this study, eBC monthly averages were larger for negative SCAN phase and smaller for positive phase, in agreement with the impact described by Stathopoulos et al. (2021). SCAN explained only 4% of the model bias variability in the cold season (Fig. S9a), indicating that the effect of such index was already captured by one of the variables included in the model, likely temperature. In fact, the average sea level pressure map associated to high surface temperature and high eBC concentration (Fig. 6a) corresponds to the SCAN negative phase pressure

430 pattern. Conversely, SCAN explained 31% of the model bias variability in the warm period (Fig. S9b). In particular, months with a strong negative SCAN index (smaller than -2) were associated to the largest monthly biases. Adding SCAN to GAM would likely help to improve GAM models in the warm period.

To test the impact of potential unaccounted synoptic-scale circulation pattern in the cold period, we first calculated the average cold season SLP map from 30 to 90 degrees north, we calculated the SLP anomalies (the difference between each

daily map and the cold period average map), and finally we investigated the correlation between the anomaly time series in each cell and the time series of the GAM model residuals (the differences between the measured eBC concentration and the eBC simulated by the cold season model). Figure 9 reports the map of the Pearson's correlation coefficients and shows that higher residuals were associated with low pressure anomalies over Scandinavia and western Russia and high pressure anomalies over the Atlantic Ocean, between Spain and the Azores. The lowest Pearson's correlation coefficient (r) between residual time series and SLP anomalies was observed in the region between $55°$ and $65°$ north and between $42°$ and $50°$ east (r=-0.21), while the highest correlation was reported for the region between $30°$ and $45°$ north and $10°$ and $22°$ west (r =0.19). We re-run the GAM model adding the SLP difference between these two regions as a predictor variable. The SLP difference did not reduce the statistical significance of the other co-variates contributing to the model, but slightly attenuated their effect. In particular, when pressure increased from 1010 and 1025 hPa, eBC decreased by 63% instead of 70%, while the temperature increase from 255 K and 265 K reduced eBC concentration by 24% instead of 32%. Finally, eBC increased by 33% instead of 40% when BLH increased from 100 m up to 600 m.

The use of SLP gradient as covariate, increased significantly the deviance explained by the model (from 47% to 52%). The eBC dependency on the pressure gradient was linear and the average eBC concentration increased by 67% when pressure difference raised from values lower than -10 hPa to higher than 20 hPa (i.e. lower pressure over western Russia and higher pressure over the Atlantic). Figure 9b reports the probability time map of the back trajectories reaching GAL when the pressure difference between the two regions was larger than 20 hPa. The map shows that for larger pressure gradients, trajectories moved over central and northern Russia before reaching the Arctic. The high pressure difference between the two regions likely accelerated the transport of air masses over southern Europe, and then the low pressure system over western Russia favoured a rapid movement of such air masses towards the Arctic. These results indicate that transport through northern Russia is a very effect pathway for pollution into the European Arctic.

The deviance explained by cold and warm season GAM were comparable to the ones previously published for models investigating particulate matter (PM) variability. For example, the deviance explained by GAM describing fine and coarse aerosol mass concentration in European urban and rural sites ranged between 28% and 75% (Barmpadimos et al., 2012), while consistently smaller values were reported in remote areas (38% - 45%) (Barmpadimos et al., 2011). eBC hourly concentrations at GAL were often of the same order of magnitude as the analytical quantification limit (2 ng m^{-3} assuming the limit of quantification equal to 10 times the blank standard deviation from Asmi et al. (2021)). As a consequence, the measurement uncertainty might reduce the fraction of variance that could be described by the model, leading to a relatively lower deviance explained (Barmpadimos et al., 2012). The mean square errors (MSE) were 2.8 ng m^{-3} and 2.6 ng m^{-3} in the cold and warm season, respectively. To investigate GAM model performance, Fig.10a and 10b report the scatter plots of modelled versus observed concentration during the two seasons. Most of the points were close to the 1-to-1 line and the fraction of data with a modelled to observed eBC ratio between 0.5 and 2 (Chang and Hanna, 2004), was equal to 72% and 71% in the cold and the warm period, respectively. GAM models underpredicted eBC during both seasons for concentrations larger than 50 ng m^{-3}, likely due to the difficulties the model has to describe the behaviour of an under-represented eBC concentration range. In fact, eBC daily average was larger than 50 ng m^{-3} only during 9% and 1% of the time in the cold and warm season, respectively.
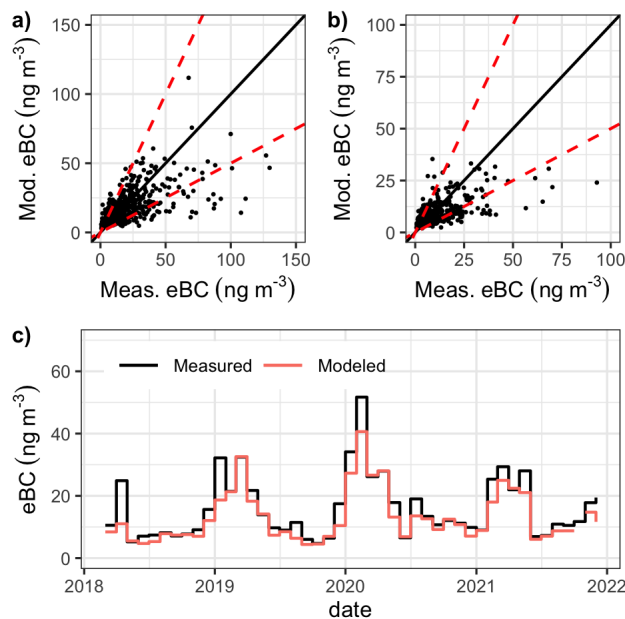
Figure 10. Comparison between measured and modelled eBC concentration during the cold (panel a) and warm (panel b) season; red dotted line indicates the factor of two area. Panel c shows the time trends of modelled and measured eBC monthly averages.

470 Figure 10c shows that overall, the model reproduces well the observed seasonal and interannual variability of the monthly eBC averages (Fig. 10c).

4 Conclusions

Black carbon is a short-lived climate forcer that plays a crucial role in the Arctic climate system. Nevertheless, most climate models still fail in reproducing its atmospheric concentration seasonal changes at high latitudes. We analyse equivalent
475 black carbon (eBC) concentration variability during four years at the Gruvebadet Atmospheric Laboratory, in the Svalbard archipelago, to understand the impact of local and synoptic scale processes on black carbon seasonality in the European Arctic.
To study eBC variability, we deployed Generalized Additive Models that allowed us to describe eBC concentration as the sum of multiple factors, each of them depending on a single covariate, without assuming a linear relationship with the predicted variable (eBC). We tested local meteorological observations, ERA5 reanalysis products, and general circulation indices as
480 covariates. Compared to previous studies that investigated the impact of a single variable or process at a time (Stathopoulos et al., 2021; Eckhardt et al., 2003), the GAM approach allowed us to evaluate simultaneously the effect of multiple variables, disentangling their relative contribution. Both cold and warm seasons eBC concentrations were equally well explained by the GAM models.

eBC concentration showed clear seasonal differences, with higher values in late winter and spring and lower concentrations in summer. We observed a weak to moderate correlation between the seasonal variabilities of eBC and removal processes, taking place at regional scale during transport from lower latitudes. We observed that precipitation amount integrated during transport is a key factor controlling aerosol seasonality, especially during the warm season, when precipitation rate is higher. On the other hand, the link between emissions variability and eBC concentration was not as clear, even if BC emission inventories were used in connection with back trajectories, to account for the changes in air mass circulation patterns. Although with some caution due to the fact that anthropogenic BC emissions were only available for a single reference year (i.e. 2018), the results presented here agree with the conclusions, based on tracer analysis, that wet scavenging controls the seasonal cycle of pollutant concentrations observed in the Arctic (Garrett et al., 2011).

Local temperature explained a significant fraction of the eBC variance, during both cold and warm periods, but with opposite effects. During the cold season, higher concentrations were observed for temperatures at GAL smaller than 265 K. Stohl (2006) reported that effective pollution transport to the Arctic lower troposphere requires the penetration of the polar Dome from sideways. This route is possible for air masses characterized by low potential temperature. 85% of the back trajectories reaching GAL during cold days experienced a diabatic cooling (potential temperature decrease) up to one day before reaching the observatory. The average cooling rate was -1.6 K day^{-1}, which is higher than the rate expected from radiative cooling, but in agreement with diabatic cooling due to contact with snow-covered ground (Stohl, 2006). This result agrees with back trajectories showing the potential impact of air masses form northern Siberia during colder days.

During the warm season, eBC concentration almost doubled when temperature increased from 275 K to 285 K. Back trajectory analysis confirms that higher temperatures in Svalbard corresponded to the intrusion of polluted and warmer air masses from lower latitudes, where BC sources are located. Warm air intrusions have been particularly investigated during winter for their contribution to reduction of sea-ice concentration and impact on cloud radiative forcing (Woods et al., 2013; Woods and Caballero, 2016; Zhang et al., 2023). On the contrary, studies of summer events are limited, although the presence of sunlight in this season makes climate implications even more complex (Tjernström et al., 2019; You et al., 2021). Recently, a few studies reported a correlation between pollution transport to the Arctic with warm-air intrusion based on the analysis of single events in summer and late spring (Bossioli et al., 2021; Dada et al., 2022). Our results verified the consistency of such pattern with longer time series and highlighted the need to further investigate the implications of warm-air intrusion in the warm periods, when background aerosol concentration is lower and these events can alter substantially aerosol population climate-relevant properties (Dada et al., 2022).

Among synoptic-scale meteorology descriptors, SCAN might contribute to the temporal eBC variability in the warm seasons, although the lack of daily time resolution for this index did not allow us to test it as a predictor in the GAM model. In the cold period, higher eBC concentration were observed for a positive pressure gradient between northern and southern Europe, that favoured the transport of polluted air masses from central and northern Russia.

In closing, eBC concentrations in the European Arctic are modulated by effective scavenging of pollution during transport (eBC reduction) and by synoptic-scale meteorological processes that promotes effective transport from lower latitudes, such as diabatic cooling of air masses moving over snow-covered ground, intrusion of warm air from lower latitudes, and specific sea

level pressure patterns. Changes of these processes exacerbated by climate change will have an impact on the pollution burden
of the future Arctic and concentration temporal variability.

Data availability. Hourly eBC and meteorological data time series from the Gruvebadet observatory are available at https://iadc.cnr.it/cnr/index.php. eBC daily data are available at https://data.iadc.cnr.it/erddap/tabledap/gilardoni_acp_ebc_2023.html, while daily meteorological data can be found at https://data.iadc.cnr.it/erddap/tabledap/gilardoni_acp_met_2023.html

Author contributions. SG designed the study, MS provided back trajectories, SG and MM acquired and analysed field measurements, SG, DHR, MM, VV, MS, and RK contributed to data discussion and interpretation

Competing interests. At least one of the (co-)authors is a member of the editorial board of Atmospheric Chemistry and Physics.

Acknowledgements. The authors would like to acknowledge the Italian National Arctic Research Programme (PRA) for financial support of the experimental activities at the Gruvebadet Atmospheric Laboratory and the Climate Change Tower. This research was funded by the Italian Ministry of University and Research (MIUR) within the framework of the Arctic Research Program through the project "BETHA-NyÅ" - Boundary layer evolution through harmonization of aerosol measurements at Ny-Ålesund research station (PRA2021-0020). We would like to thank Ari Virkkula for the profitable discussion on the PSAP correction algorithm, The Svalbard Integrated Observing System network for promoting collaboration and discussion at Ny-Ålesund, and personnel at Gruvebadet Atmospheric Laboratory for support during field measurements. A special acknowledge to Angelo Viola, who continuously supported the field work at Gruvebadet with high dedication and commitment.

References

Akagi, S. K., Yokelson, R. J., Wiedinmyer, C., Alvarado, M. J., Reid, J. S., Karl, T., Crounse, J. D., and Wennberg, P. O.: Emission factors for open and domestic biomass burning for use in atmospheric models, Atmospheric Chemistry and Physics, 11, 4039–4072, https://doi.org/10.5194/acp-11-4039-2011, 2011.

Albrecht, B. A.: Aerosols, cloud microphysics, and fractional cloudiness., Science, 245, 1227–1230, https://doi.org/10.1126/science.245.4923.1227, 1989.

Andreae, M. O. and Merlet, P.: Emission of trace gases and aerosols from biomass burning, Global Biogeochemical Cycles, 15, 955–966, https://doi.org/https://doi.org/10.1029/2000GB001382, 2001.

Ashbaugh, L. L., Malm, W. C., and Sadeh, W. Z.: A residence time probability analysis of sulfur concentrations at grand Canyon National Park, Atmospheric Environment (1967), 19, 1263–1270, https://doi.org/https://doi.org/10.1016/0004-6981(85)90256-2, 1985.

Asmi, E., Backman, J., Servomaa, H., Virkkula, A., Gini, M. I., Eleftheriadis, K., Müller, T., Ohata, S., Kondo, Y., and Hyvärinen, A.: Absorption instruments inter-comparison campaign at the Arctic Pallas station, Atmospheric Measurement Techniques, 14, 5397–5413, https://doi.org/10.5194/amt-14-5397-2021, 2021.

Backman, J., Schmeisser, L., and Asmi, E.: Asian Emissions Explain Much of the Arctic Black Carbon Events, Geophysical Research Letters, 48, e2020GL091 913, https://doi.org/https://doi.org/10.1029/2020GL091913, e2020GL091913 2020GL091913, 2021.

Barmpadimos, I., Hueglin, C., Keller, J., Henne, S., and Prévôt, A. S. H.: Influence of meteorology on PM_{10} trends and variability in Switzerland from 1991 to 2008, Atmospheric Chemistry and Physics, 11, 1813–1835, https://doi.org/10.5194/acp-11-1813-2011, 2011.

Barmpadimos, I., Keller, J., Oderbolz, D., Hueglin, C., and Prévôt, A. S. H.: One decade of parallel fine (PM2.5) and coarse (PM10–PM2.5) particulate matter measurements in Europe: trends and variability, Atmospheric Chemistry and Physics, 12, 3189–3203, 2012.

Barnston, A. G. and Livezey, R. E.: Classification, Seasonality and Persistence of Low-Frequency Atmospheric Circulation Patterns, Monthly Weather Review, 115, 1083 – 1126, https://doi.org/https://doi.org/10.1175/1520-0493(1987)115<1083:CSAPOL>2.0.CO;2, 1987.

Binder, H., Boettcher, M., Grams, C. M., Joos, H., Pfahl, S., and Wernli, H.: Exceptional Air Mass Transport and Dynamical Drivers of an Extreme Wintertime Arctic Warm Event, Geophysical Research Letters, 44, 12,028–12,036, https://doi.org/https://doi.org/10.1002/2017GL075841, 2017.

Bond, T. C., Anderson, T. L., and Campbell, D.: Calibration and Intercomparison of Filter-Based Measurements of Visible Light Absorption by Aerosols, Aerosol Science and Technology, 30, 582–600, 1999.

Bond, T. C., Doherty, S. J., Fahey, D. W., Forster, P. M., Berntsen, T., DeAngelo, B. J., Flanner, M. G., Ghan, S., Kärcher, B., Koch, D., Kinne, S., Kondo, Y., Quinn, P. K., Sarofim, M. C., Schultz, M. G., Schulz, M., Venkataraman, C., Zhang, H., Zhang, S., Bellouin, N., Guttikunda, S. K., Hopke, P. K., Jacobson, M. Z., Kaiser, J. W., Klimont, Z., Lohmann, U., Schwarz, J. P., Shindell, D., Storelvmo, T., Warren, S. G., and Zender, C. S.: Bounding the role of black carbon in the climate system: A scientific assessment, Journal of Geophysical Research: Atmospheres, p. doi:10.1002/jgrd.50171, 2013.

Bossioli, E., Sotiropoulou, G., Methymaki, G., and Tombrou, M.: Modeling Extreme Warm-Air Advection in the Arctic During Summer: The Effect of Mid-Latitude Pollution Inflow on Cloud Properties, Journal of Geophysical Research: Atmospheres, 126, e2020JD033 291, https://doi.org/https://doi.org/10.1029/2020JD033291, e2020JD033291 2020JD033291, 2021.

Browse, J., Carslaw, K. S., Arnold, S. R., Pringle, K., and Boucher, O.: The scavenging processes controlling the seasonal cycle in Arctic sulphate and black carbon aerosol, Atmospheric Chemistry and Physics, 12, 6775–6798, https://doi.org/10.5194/acp-12-6775-2012, 2012.

Chang, J. C. and Hanna, S. R.: Air quality model performance evaluation, Meteorology and Atmospheric Physics, 87, 167–196, https://doi.org/10.1007/s00703-003-0070-7, 2004.

Chen, X., Kang, S., and Yang, J.: Investigation of distribution, transportation, and impact factors of atmospheric black carbon in the Arctic region based on a regional climate-chemistry model, Environmental Pollution, 257, 113 127, https://doi.org/https://doi.org/10.1016/j.envpol.2019.113127, 2020.

Christoudias, T., Pozzer, A., and Lelieveld, J.: Influence of the North Atlantic Oscillation on air pollution transport, Atmospheric Chemistry and Physics, 12, 869–877, https://doi.org/10.5194/acp-12-869-2012, 2012.

Clifford, S., Low Choy, S., Hussein, T., Mengersen, K., and Morawska, L.: Using the Generalised Additive Model to model the particle number count of ultrafine particles, Atmospheric Environment, 45, 5934–5945, https://doi.org/https://doi.org/10.1016/j.atmosenv.2011.05.004, 2011.

Crawford, J., Chambers, S., Cohen, D. D., Williams, A., Griffiths, A., Stelcer, E., and Dyer, L.: Impact of meteorology on fine aerosols at Lucas Heights, Australia, Atmospheric Environment, 145, 135–146, https://doi.org/https://doi.org/10.1016/j.atmosenv.2016.09.025, 2016.

Cremer, R. S., Tunved, P., and Ström, J.: Airmass Analysis of Size-Resolved Black Carbon Particles Observed in the Arctic Based on Cluster Analysis, Atmosphere, 13, https://doi.org/10.3390/atmos13050648, 2022.

Crippa, M., Oreggioni, G., Guizzardi, D., Muntean, M., Schaaf, E., Lo Vullo, E., Solazzo, E., Monforti-Ferrario, F., Olivier, J. G. J., and E., V.: Fossil CO2 and GHG emissions of all world countries, Tech. rep., Publications Office of the European Union, 2019.

Dada, L., Angot, H., Beck, I., Baccarini, A., Quéléver, L. L. J., Boyer, M., Laurila, T., Brasseur, Z., Jozef, G., de Boer, G., Shupe, M. D., Henning, S., Bucci, S., Dütsch, M., Stohl, A., Petäjä, T., Daellenbach, K. R., Jokinen, T., and Schmale, J.: A central arctic extreme aerosol event triggered by a warm air-mass intrusion, Nature Communications, 13, 5290, https://doi.org/10.1038/s41467-022-32872-2, 2022.

Dekhtyareva, A., Hermanson, M., Nikulina, A., Hermansen, O., Svendby, T., Holmén, K., and Graversen, R. G.: Springtime nitrogen oxides and tropospheric ozone in Svalbard: results from the measurement station network, Atmospheric Chemistry and Physics, 22, 11 631–11 656, https://doi.org/10.5194/acp-22-11631-2022, 2022.

Eckhardt, S., Stohl, A., Beirle, S., Spichtinger, N., James, P., Forster, C., Junker, C., Wagner, T., Platt, U., and Jennings, S. G.: The North Atlantic Oscillation controls air pollution transport to the Arctic, Atmospheric Chemistry and Physics, 3, 1769–1778, https://doi.org/10.5194/acp-3-1769-2003, 2003.

Eleftheriadis, K., Vratolis, S., and Nyeki, S.: Aerosol black carbon in the European Arctic: measurements at Zeppelin station, Ny-Ålesund, Svalbard from 1998–2007, Geophysical Research Letters, 36, 2009.

Evangeliou, N., Balkanski, Y., Hao, W. M., Petkov, A., Silverstein, R. P., Corley, R., Nordgren, B. L., Urbanski, S. P., Eckhardt, S., Stohl, A., Tunved, P., Crepinsek, S., Jefferson, A., Sharma, S., Nøjgaard, J. K., and Skov, H.: Wildfires in northern Eurasia affect the budget of black carbon in the Arctic – a 12-year retrospective synopsis (2002–2013), Atmospheric Chemistry and Physics, 16, 7587–7604, https://doi.org/10.5194/acp-16-7587-2016, 2016.

Flanner, M. G.: Arctic climate sensitivity to local black carbon, Journal of Geophysical Research: Atmospheres, 118, 1840–1851, https://doi.org/https://doi.org/10.1002/jgrd.50176, 2013.

Flanner, M. G., Zender, C. S., Randerson, J. T., and Rasch, P. J.: Present-day climate forcing and response from black carbon in snow, Journal of Geophysical Research: Atmospheres, 112, https://doi.org/https://doi.org/10.1029/2006JD008003, 2007.

Freud, E., Krejci, R., Tunved, P., Leaitch, R., Nguyen, Q. T., Massling, A., Skov, H., and Barrie, L.: Pan-Arctic aerosol number size distributions: seasonality and transport patterns, Atmospheric Chemistry and Physics, 17, 8101–8128, https://doi.org/10.5194/acp-17-8101-2017, 2017.

Garrett, T. J., Brattström, S., Sharma, S., Worthy, D. E. J., and Novelli, P.: The role of scavenging in the seasonal transport of black carbon and sulfate to the Arctic, Geophysical Research Letters, 38, https://doi.org/https://doi.org/10.1029/2011GL048221, 2011.

Graßl, S., Ritter, C., and Schulz, A.: The Nature of the Ny-Alesund Wind Field Analysed by High-Resolution Windlidar Data, Remote Sensing, 14, https://doi.org/10.3390/rs14153771, 2022.

Hanna, E., Fettweis, X., Mernild, S. H., Cappelen, J., Ribergaard, M. H., Shuman, C. A., Steffen, K., Wood, L., and Mote, T. L.: Atmospheric and oceanic climate forcing of the exceptional Greenland ice sheet surface melt in summer 2012, International Journal of Climatology, 34, 1022–1037, https://doi.org/https://doi.org/10.1002/joc.3743, 2014.

Hansen, J. and Nazarenko, L.: Soot climate forcing via snow and ice albedos, Proceedings of the National Academy of Sciences, 101, 423–428, https://doi.org/10.1073/pnas.2237157100, 2004.

Hansen, J., Sato, M., Ruedy, R., Nazarenko, L., Lacis, A., Schmidt, G. A., Russell, G., Aleinov, I., Bauer, M., Bauer, S., Bell, N., Cairns, B., Canuto, V., Chandler, M., Cheng, Y., Del Genio, A., Faluvegi, G., Fleming, E., Friend, A., Hall, T., Jackman, C., Kelley, M., Kiang, N., Koch, D., Lean, J., Lerner, J., Lo, K., Menon, S., Miller, R., Minnis, P., Novakov, T., Oinas, V., Perlwitz, J., Perlwitz, J., Rind, D., Romanou, A., Shindell, D., Stone, P., Sun, S., Tausnev, N., Thresher, D., Wielicki, B., Wong, T., Yao, M., and Zhang, S.: Efficacy of climate forcings, Journal of Geophysical Research: Atmospheres, 110, https://doi.org/https://doi.org/10.1029/2005JD005776, 2005.

Hastie, T. and Tibshirani, R.: Generalized Additive Models, vol. 1, Institute of Mathematical Statistics, http://www.jstor.org/stable/2245459, 1986.

Hersbach, H., Bell, B., Berrisford, P., Hirahara, S., Horányi, A., Muñoz-Sabater, J., Nicolas, J., Peubey, C., Radu, R., Schepers, D., Simmons, A., Soci, C., Abdalla, S., Abellan, X., Balsamo, G., Bechtold, P., Biavati, G., Bidlot, J., Bonavita, M., De Chiara, G., Dahlgren, P., Dee, D., Diamantakis, M., Dragani, R., Flemming, J., Forbes, R., Fuentes, M., Geer, A., Haimberger, L., Healy, S., Hogan, R. J., Hólm, E., Janisková, M., Keeley, S., Laloyaux, P., Lopez, P., Lupu, C., Radnoti, G., de Rosnay, P., Rozum, I., Vamborg, F., Villaume, S., and Thépaut, J.-N.: The ERA5 global reanalysis, Quarterly Journal of the Royal Meteorological Society, 146, 1999–2049, https://doi.org/https://doi.org/10.1002/qj.3803, 2020.

Huang, K., Fu, J. S., Prikhodko, V. Y., Storey, J. M., Romanov, A., Hodson, E. L., Cresko, J., Morozova, I., Ignatieva, Y., and Cabaniss, J.: Russian anthropogenic black carbon: Emission reconstruction and Arctic black carbon simulation, Journal of Geophysical Research: Atmospheres, 120, 11,306–11,333, https://doi.org/https://doi.org/10.1002/2015JD023358, 2015.

Hurrell, J. W.: Decadal Trends in the North Atlantic Oscillation: Regional Temperatures and Precipitation, Science, 269, 676–679, https://doi.org/10.1126/science.269.5224.676, 1995.

Jackson, L. S., Carslaw, N., Carslaw, D. C., and Emmerson, K. M.: Modelling trends in OH radical concentrations using generalized additive models, Atmospheric Chemistry and Physics, 9, 2021–2033, https://doi.org/10.5194/acp-9-2021-2009, 2009.

Koch, D., Schulz, M., Kinne, S., McNaughton, C., Spackman, J. R., Balkanski, Y., Bauer, S., Berntsen, T., Bond, T. C., Boucher, O., Chin, M., Clarke, A., De Luca, N., Dentener, F., Diehl, T., Dubovik, O., Easter, R., Fahey, D. W., Feichter, J., Fillmore, D., Freitag, S., Ghan, S., Ginoux, P., Gong, S., Horowitz, L., Iversen, T., Kirkevag;g, A., Klimont, Z., Kondo, Y., Krol, M., Liu, X., Miller, R., Montanaro, V., Moteki, N., Myhre, G., Penner, J. E., Perlwitz, J., Pitari, G., Reddy, S., Sahu, L., Sakamoto, H., Schuster, G., Schwarz, J. P., Seland, O., Stier, P., Takegawa, N., Takemura, T., Textor, C., van Aardenne, J. A., and Zhao, Y.: Evaluation of black carbon estimations in global aerosol models, Atmospheric Chemistry and Physics, 9, 9001–9026, https://doi.org/10.5194/acp-9-9001-2009, 2009.

Lund, M. T., Berntsen, T. K., and Samset, B. H.: Sensitivity of black carbon concentrations and climate impact to aging and scavenging in OsloCTM2–M7, Atmospheric Chemistry and Physics, 17, 6003–6022, 2017.

Lund, M. T., Myhre, G., Haslerud, A. S., Skeie, R. B., Griesfeller, J., Platt, S. M., Kumar, R., Myhre, C. L., and Schulz, M.: Concentrations and radiative forcing of anthropogenic aerosols from 1750 to 2014 simulated with the Oslo CTM3 and CEDS emission inventory, Geoscientific Model Development, 11, 4909–4931, https://doi.org/10.5194/gmd-11-4909-2018, 2018.

Maturilli, M. and Kayser, M.: Arctic warming, moisture increase and circulation changes observed in the Ny-Ålesund homogenized radiosonde record, Theoretical and Applied Climatology, 130, 1–17, https://doi.org/10.1007/s00704-016-1864-0, 2017.

Maturilli, M., Herber, A., and König-Langlo, G.: Climatology and time series of surface meteorology in Ny-Ålesund, Svalbard, Earth System Science Data, 5, 155–163, https://doi.org/10.5194/essd-5-155-2013, 2013.

Mazzola, M., Busetto, M., Ferrero, L., Viola, A. P., and Cappelletti, D.: AGAP: an atmospheric gondola for aerosol profiling, Rendiconti Lincei, 27, 105–113, 2016.

Müller, T., Nowak, A., Wiedensohler, A., Sheridan, P., Laborde, M., Covert, D. S., Marinoni, A., Imre, K., Henzing, B., Roger, J.-C., dos Santos, S. M., Wilhelm, R., Wang, Y.-Q., and de Leeuw, G.: Angular Illumination and Truncation of Three Different Integrating Nephelometers: Implications for Empirical, Size-Based Corrections, Aerosol Science and Technology, 43, 581–586, https://doi.org/10.1080/02786820902798484, 2009.

Müller, T., Laborde, M., Kassell, G., and Wiedensohler, A.: Design and performance of a three-wavelength LED-based total scatter and backscatter integrating nephelometer, Atmospheric Measurement Techniques, 4, 1291–1303, 2011.

Nystuen, J. A.: Relative Performance of Automatic Rain Gauges under Different Rainfall Conditions, Journal of Atmospheric and Oceanic Technology, 16, 1025 – 1043, https://doi.org/https://doi.org/10.1175/1520-0426(1999)016<1025:RPOARG>2.0.CO;2, 1999.

Ogren, J. A.: Comment on "Calibration and Intercomparison of Filter-Based Measurements of Visible Light Absorption by Aerosols", Aerosol Science and Technology, 44, 589–591, https://doi.org/10.1080/02786826.2010.482111, 2010.

Ohata, S., Mori, T., Kondo, Y., Sharma, S., Hyvärinen, A., Andrews, E., Tunved, P., Asmi, E., Backman, J., Servomaa, H., Veber, D., Eleftheriadis, K., Vratolis, S., Krejci, R., Zieger, P., Koike, M., Kanaya, Y., Yoshida, A., Moteki, N., Zhao, Y., Tobo, Y., Matsushita, J., and Oshima, N.: Estimates of mass absorption cross sections of black carbon for filter-based absorption photometers in the Arctic, Atmospheric Measurement Techniques, 14, 6723–6748, https://doi.org/10.5194/amt-14-6723-2021, 2021.

Papritz, L.: Arctic Lower-Tropospheric Warm and Cold Extremes: Horizontal and Vertical Transport, Diabatic Processes, and Linkage to Synoptic Circulation Features, Journal of Climate, 33, 993 – 1016, https://doi.org/https://doi.org/10.1175/JCLI-D-19-0638.1, 2020.

Pasquier, J. T., David, R. O., Freitas, G., Gierens, R., Gramlich, Y., Haslett, S., Li, G., Schäfer, B., Siegel, K., Wieder, J., Adachi, K., Belosi, F., Carlsen, T., Decesari, S., Ebell, K., Gilardoni, S., Gysel-Beer, M., Henneberger, J., Inoue, J., Kanji, Z. A., Koike, M., Kondo, Y., Krejci, R., Lohmann, U., Maturilli, M., Mazzolla, M., Modini, R., Mohr, C., Motos, G., Nenes, A., Nicosia, A., Ohata, S., Paglione, M., Park, S., Pileci, R. E., Ramelli, F., Rinaldi, M., Ritter, C., Sato, K., Storelvmo, T., Tobo, Y., Traversi, R., Viola, A., and Zieger, P.: The Ny-Ålesund Aerosol Cloud Experiment (NASCENT): Overview and First Results, Bulletin of the American Meteorological Society, 103, E2533 – E2558, https://doi.org/https://doi.org/10.1175/BAMS-D-21-0034.1, 2022.

Petzold, A. and Schönlinner, M.: Multi-angle absorption photometry—a new method for the measurement of aerosol light absorption and atmospheric black carbon, Journal of Aerosol Science, 35, 421–441, 2004.

Petzold, A., Ogren, J. A., Fiebig, M., Laj, P., Li, S.-M., Baltensperger, U., Holzer-Popp, T., Kinne, S., Pappalardo, G., Sugimoto, N., et al.: Recommendations for reporting" black carbon" measurements, Atmospheric Chemistry and Physics, 13, 8365–8379, 2013.

Popovicheva, O. B., Evangeliou, N., Kobelev, V. O., Chichaeva, M. A., Eleftheriadis, K., Gregorič, A., and Kasimov, N. S.: Siberian Arctic black carbon: gas flaring and wildfire impact, Atmospheric Chemistry and Physics, 22, 5983–6000, https://doi.org/10.5194/acp-22-5983-2022, 2022.

Quinn, P., Stohl, A., Arneth, A., Berntsen, T., Burkhart, J. F., Christensen, J., Flanner, M. G., Kupiainen, K., Lihavainen, H., Shepherd, M., Shevchenko, V., Skov, H., and Vestrng, V.: The Impact of Black Carbon on Arctic Climate, Tech. rep., Arctic Monitoring and Assessment Programme, 2011.

Quinn, P. K., Bates, T. S., Coffman, D. J., and Covert, D. S.: Influence of particle size and chemistry on the cloud nucleating properties of aerosols, Atmospheric Chemistry and Physics, 8, 1029–1042, https://doi.org/10.5194/acp-8-1029-2008, 2008.

Quinn, P. K., Stohl, A., Arnold, S., Baklanov, A., Berntsen, T., Christensen, J., Eckhardt, S., Flanner, M. G., Klimont, Z., Korsholm, s., Kupiainen, K., Langner, J., Law, K., Monks, S., von Salzen, K., Sand, M., Schmale, J., and Vestreng, V.: Black carbon and ozone as Arctic climate forcers, Tech. rep., Arctic Monitoring and Assessment Programme, 2015.

Rader, F., Traversi, R., Severi, M., Becagli, S., Müller, K.-J., Nakoudi, K., and Ritter, C.: Overview of Aerosol Properties in the European Arctic in Spring 2019 Based on In Situ Measurements and Lidar Data, Atmosphere, 12, https://doi.org/10.3390/atmos12020271, 2021.

Randerson, J. T., Chen, Y., van der Werf, G. R., Rogers, B. M., and Morton, D. C.: Global burned area and biomass burning emissions from small fires, Journal of Geophysical Research: Biogeosciences, 117, https://doi.org/https://doi.org/10.1029/2012JG002128, 2012.

Rose, C., Collaud Coen, M., Andrews, E., Lin, Y., Bossert, I., Lund Myhre, C., Tuch, T., Wiedensohler, A., Fiebig, M., Aalto, P., Alastuey, A., Alonso-Blanco, E., Andrade, M., Artíñano, B., Arsov, T., Baltensperger, U., Bastian, S., Bath, O., Beukes, J. P., Brem, B. T., Bukowiecki, N., Casquero-Vera, J. A., Conil, S., Eleftheriadis, K., Favez, O., Flentje, H., Gini, M. I., Gómez-Moreno, F. J., Gysel-Beer, M., Hallar, A. G., Kalapov, I., Kalivitis, N., Kasper-Giebl, A., Keywood, M., Kim, J. E., Kim, S.-W., Kristensson, A., Kulmala, M., Lihavainen, H., Lin, N.-H., Lyamani, H., Marinoni, A., Martins Dos Santos, S., Mayol-Bracero, O. L., Meinhardt, F., Merkel, M., Metzger, J.-M., Mihalopoulos, N., Ondracek, J., Pandolfi, M., Pérez, N., Petäjä, T., Petit, J.-E., Picard, D., Pichon, J.-M., Pont, V., Putaud, J.-P., Reisen, F., Sellegri, K., Sharma, S., Schauer, G., Sheridan, P., Sherman, J. P., Schwerin, A., Sohmer, R., Sorribas, M., Sun, J., Tulet, P., Vakkari, V., van Zyl, P. G., Velarde, F., Villani, P., Vratolis, S., Wagner, Z., Wang, S.-H., Weinhold, K., Weller, R., Yela, M., Zdimal, V., and Laj, P.: Seasonality of the particle number concentration and size distribution: a global analysis retrieved from the network of Global Atmosphere Watch (GAW) near-surface observatories, Atmospheric Chemistry and Physics, 21, 17 185–17 223, https://doi.org/10.5194/acp-21-17185-2021, 2021.

Sand, M., Berntsen, T. K., Kay, J. E., Lamarque, J. F., Seland, Ø., and Kirkevåg, A.: The Arctic response to remote and local forcing of black carbon, Atmospheric Chemistry and Physics, 13, 211–224, https://doi.org/10.5194/acp-13-211-2013, 2013.

Sand, M., Berntsen, T., Von Salzen, K., Flanner, M., Langner, J., and Victor, D.: Response of Arctic temperature to changes in emissions of short-lived climate forcers, Nature Climate Change, 6, 286, 2016.

Schmale, J., Sharma, S., Decesari, S., Pernov, J., Massling, A., Hansson, H.-C., von Salzen, K., Skov, H., Andrews, E., Quinn, P. K., Upchurch, L. M., Eleftheriadis, K., Traversi, R., Gilardoni, S., Mazzola, M., Laing, J., and Hopke, P.: Pan-Arctic seasonal cycles and long-term trends of aerosol properties from 10 observatories, Atmospheric Chemistry and Physics, 22, 3067–3096, https://doi.org/10.5194/acp-22-3067-2022, 2022.

Schmeisser, L., Backman, J., Ogren, J. A., Andrews, E., Asmi, E., Starkweather, S., Uttal, T., Fiebig, M., Sharma, S., Eleftheriadis, K., et al.: Seasonality of aerosol optical properties in the Arctic, Atmospheric Chemistry and Physics, 18, 11 599–11 622, 2018.

Sharma, N., Arnold, I. J., Moosmüller, H., Arnott, W. P., and Mazzoleni, C.: Photoacoustic and nephelometric spectroscopy of aerosol optical properties with a supercontinuum light source, Atmos. Meas. Tech., 6, 3501–3513, https://doi.org/10.5194/amt-6-3501-2013, 2013.

Shindell, D. T., Chin, M., Dentener, F., Doherty, R. M., Faluvegi, G., Fiore, A. M., Hess, P., Koch, D. M., MacKenzie, I. A., Sanderson, M. G., Schultz, M. G., Schulz, M., Stevenson, D. S., Teich, H., Textor, C., Wild, O., Bergmann, D. J., Bey, I., Bian, H., Cuvelier, C., Duncan, B. N., Folberth, G., Horowitz, L. W., Jonson, J., Kaminski, J. W., Marmer, E., Park, R., Pringle, K. J., Schroeder, S., Szopa, S., Takemura,

T., Zeng, G., Keating, T. J., and Zuber, A.: A multi-model assessment of pollution transport to the Arctic, Atmospheric Chemistry and Physics, 8, 5353–5372, https://doi.org/10.5194/acp-8-5353-2008, 2008.

Sjöblom, A., Esau, I., and Repina, I.: Wind Climate in Kongsfjorden, Svalbard, and Attribution of Leading Wind Driving Mechanisms through Turbulence-Resolving Simulations, Advances in Meteorology, 2012, 568 454, https://doi.org/10.1155/2012/568454, 2012.

Song, C., Dall'Osto, M., Lupi, A., Mazzola, M., Traversi, R., Becagli, S., Gilardoni, S., Vratolis, S., Yttri, K. E., Beddows, D. C. S., Schmale, J., Brean, J., Kramawijaya, A. G., Harrison, R. M., and Shi, Z.: Differentiation of coarse-mode anthropogenic, marine and dust particles in the High Arctic islands of Svalbard, Atmospheric Chemistry and Physics, 21, 11 317–11 335, https://doi.org/10.5194/acp-21-11317-2021, 2021.

Sprenger, M. and Wernli, H.: The LAGRANTO Lagrangian analysis tool – version 2.0, Geoscientific Model Development, 8, 2569–2586, https://doi.org/10.5194/gmd-8-2569-2015, 2015.

Srivastava, R. and Ravichandran, M.: Spatial and seasonal variations of black carbon over the Arctic in a regional climate model, Polar Science, 30, 100 670, https://doi.org/https://doi.org/10.1016/j.polar.2021.100670, special Issue on "Polar Studies - Window to the changing Earth", 2021.

Stathopoulos, V. K., Evangeliou, N., Stohl, A., Vratolis, S., Matsoukas, C., and Eleftheriadis, K.: Large Circulation Patterns Strongly Modulate Long-Term Variability of Arctic Black Carbon Levels and Areas of Origin, Geophysical Research Letters, 48, e2021GL092 876, https://doi.org/https://doi.org/10.1029/2021GL092876, e2021GL092876 2021GL092876, 2021.

Stohl, A.: Characteristics of atmospheric transport into the Arctic troposphere, Journal of Geophysical Research: Atmospheres, 111, https://doi.org/https://doi.org/10.1029/2005JD006888, 2006.

Stohl, A., Klimont, Z., Eckhardt, S., Kupiainen, K., Shevchenko, V. P., Kopeikin, V. M., and Novigatsky, A. N.: Black carbon in the Arctic: the underestimated role of gas flaring and residential combustion emissions, Atmospheric Chemistry and Physics, 13, 8833–8855, https://doi.org/10.5194/acp-13-8833-2013, 2013.

Szopa, S., Naik, V., Adhikary, B., Artaxo, P., Berntsen, T., Collins, W., Fuzzi, S., Gallardo, L., Kiendler-Scharr, A., Klimont, Z., Liao, H., Unger, N., and Zanis, P.: Climate Change 2021: The Physical Science Basis. Contribution of Working Group I to the Sixth Assessment Report of the Intergovernmental Panel on Climate Change, Cambridge University Press, 2021.

Tjernström, M., Shupe, M. D., Brooks, I. M., Achtert, P., Prytherch, J., and Sedlar, J.: Arctic Summer Airmass Transformation, Surface Inversions, and the Surface Energy Budget, Journal of Climate, 32, 769 – 789, https://doi.org/https://doi.org/10.1175/JCLI-D-18-0216.1, 2019.

Twomey, S.: Pollution and the planetary albedo, Atmospheric Environment (1967), 8, 1251–1256, https://doi.org/https://doi.org/10.1016/0004-6981(74)90004-3, 1974.

van der Werf, G. R., Randerson, J. T., Giglio, L., van Leeuwen, T. T., Chen, Y., Rogers, B. M., Mu, M., van Marle, M. J. E., Morton, D. C., Collatz, G. J., Yokelson, R. J., and Kasibhatla, P. S.: Global fire emissions estimates during 1997–2016, Earth System Science Data, 9, 697–720, https://doi.org/10.5194/essd-9-697-2017, 2017.

Virkkula, A.: Correction of the calibration of the 3-wavelength Particle Soot Absorption Photometer (3λ PSAP), Aerosol Science and Technology, 44, 706–712, 2010.

Wernli, H.: A Lagrangian-based analysis of extratropical cyclones. II: A detailed case-study, Quarterly Journal of the Royal Meteorological Society, 123, 1677–1706, https://doi.org/https://doi.org/10.1002/qj.49712354211, 1997.

Winiger, P., Andersson, A., Eckhardt, S., Stohl, A., and Gustafsson, Ö.: The sources of atmospheric black carbon at a European gateway to the Arctic, Nature Communications, 7, 12 776, https://doi.org/10.1038/ncomms12776, 2016.

760   Winiger, P., Andersson, A., Eckhardt, S., Stohl, A., Semiletov, I. P., Dudarev, O. V., Charkin, A., Shakhova, N., Klimont, Z., Heyes, C., et al.: Siberian Arctic black carbon sources constrained by model and observation, Proceedings of the National Academy of Sciences, 114, E1054–E1061, 2017.

Winiger, P., Barrett, T., Sheesley, R., Huang, L., Sharma, S., Barrie, L. A., Yttri, K. E., Evangeliou, N., Eckhardt, S., Stohl, A., et al.: Source apportionment of circum-Arctic atmospheric black carbon from isotopes and modeling, Science advances, 5, eaau8052, 2019.

765   Wood, S.: Generalized Additive Models, Chapman and Hall/CRC, 2017.

Woods, C. and Caballero, R.: The Role of Moist Intrusions in Winter Arctic Warming and Sea Ice Decline, Journal of Climate, 29, 4473 – 4485, https://doi.org/https://doi.org/10.1175/JCLI-D-15-0773.1, 2016.

Woods, C., Caballero, R., and Svensson, G.: Large-scale circulation associated with moisture intrusions into the Arctic during winter, Geophysical Research Letters, 40, 4717–4721, https://doi.org/https://doi.org/10.1002/grl.50912, 2013.

770   You, C., Tjernström, M., and Devasthale, A.: Eulerian and Lagrangian views of warm and moist air intrusions into summer Arctic, Atmospheric Research, 256, 105 586, https://doi.org/https://doi.org/10.1016/j.atmosres.2021.105586, 2021.

You, C., Tjernström, M., and Devasthale, A.: Warm and moist air intrusions into the winter Arctic: a Lagrangian view on the near-surface energy budgets, Atmospheric Chemistry and Physics, 22, 8037–8057, https://doi.org/10.5194/acp-22-8037-2022, 2022.

Zhang, P., Chen, G., Ting, M., Ruby Leung, L., Guan, B., and Li, L.: More frequent atmospheric rivers slow the seasonal recovery of Arctic
775   sea ice, Nature Climate Change, 13, 266–273, https://doi.org/10.1038/s41558-023-01599-3, 2023.

Zhou, C., Penner, J. E., Flanner, M. G., Bisiaux, M. M., Edwards, R., and McConnell, J. R.: Transport of black carbon to polar regions: Sensitivity and forcing by black carbon, Geophysical Research Letters, 39, https://doi.org/https://doi.org/10.1029/2012GL053388, 2012.